Published in final edited form as:
Biomaterials. 2014 July ; 35(22): 5637–5646. doi:10.1016/j.biomaterials.2014.03.076.

A Comparison of Neuroinflammation to Implanted Microelectrodes in Rat and Mouse Models

Kelsey A. Potter-Baker[a,b,1], **Madhumitha Ravikumar**[a,b,1], **Alan A. Burke**[a], **William D. Meador**[a], **Kyle T. Householder**[a,b], **Amy C. Buck**[a,b], **Smrithi Sunil**[a,b], **Wade G. Stewart**[a], **Jake P. Anna**[a], **William H. Tomaszewski**[a], and **Jeffrey R. Capadona**[a,b,*]

[a]Department of Biomedical Engineering, Case Western Reserve University, 2071 Martin Luther King Jr Drive, Wickenden Bldg., Cleveland, OH 44106, USA

[b]Advanced Platform Technology Center, L. Stokes Cleveland VA Medical Center, 10701 East Blvd. Mail Stop 151 AW/APT, Cleveland, OH 44106-1702, USA

Abstract

Rat models have emerged as a common tool to study neuroinflammation to intracortical microelectrodes. While a number of studies have attempted to understand the factors resulting in neuroinflammation using rat models, a complete understanding of key mechanistic pathways remains elusive. Transgenic mouse models, however, could facilitate a deeper understanding of mechanistic pathways due to an ease of genetic alteration. Therefore, the goal of the present study is to compare neuroinflammation following microelectrode implantation s between the rat and the mouse model. Our study suggests that subtle differences in the classic neuroinflammatory markers exist between the animal models at both two and sixteen weeks post implantation. Most notably, neuronal densities surrounding microelectrodes were significantly lower in the rat model at two weeks, while similar densities were observed between the animal models at sixteen weeks. Physiological differences between the species and slight alterations in surgical methods are likely key contributors to the observed differences. Moving forward, we propose that differences in the time course of neuroinflammation between the animal models should be considered when trying to understand and prevent intracortical microelectrode failure.

Keywords

animal models; microelectrode; brain; neuroinflammation

[*]Denotes Corresponding author; Direct correspondence to: Jeffrey R. Capadona, Ph.D., Case Western Reserve University, 2071 Martin Luther King Jr. Drive, Cleveland, OH, 44107, jeffrey.capadona@case.edu, Office: (216) 368-5486, Fax: (216) 368-1509.
[1]Denotes Co-first author

The authors have no conflicts of interest related to this work to disclose.

1. Introduction

Intracortical microelectrode technology has emerged as a promising tool in both basic neuroscience and functional rehabilitation [1, 2]. For example, intracortical microelectrodes have been utilized to functionally map neuronal circuits that may play a role in the progression of neurological diseases [3-6]. Additionally, intracortical microelectrodes have the potential to record neuronal signals, which can be translated into functional outputs such as moving a prosthetic device or computer cursor [7-9]. Unfortunately, long-term clinical use of microelectrode technology is limited primarily due to chronic device instability [10-12]. To this end, multiple studies have been conducted to better understand the failure modes of intracortical microelectrodes. Specifically, recent studies by Prasad et al. and Barrese et al. have suggested a dominant role of neuroinflammation directly contributing to mechanical, material and biological failure modes following microelectrode implantation [12-14].

Given the correlation between the neuroinflammation and device failure, several groups have begun to implicate the role of individual or small groups of pro-inflammatory molecules in facilitating neurodegeneration, device corrosion, or the propagation of the neuroinflammatory response [11, 15-21]. For example, Karumbaiah *et al.* and Moshayedi *et al.* each utilized quantitative PCR to identify specific genes (IL-36Ra and TLR-4, respectively) that were up-regulated following microglia responses to increased tissue strain [16, 17]. Skousen *et al.* demonstrated the potential correlation between tumor necrosis factor – alpha (TNFα) and neuronal loss at the microelectrode/tissue interface using both computer models and histological assessment of rats implanted with microelectrodes [18]. Furthermore, Potter *et al.* recently provided a correlation between reactive oxygen species accumulation and the up-regulation of TLR-4 and catalase combined with increased neurodegeneration [19]. While each of these studies suggested a correlation between a specific inflammatory gene or pathway and neuroinflammation, none are capable of determining definitive conclusions regarding the temporal relationship between an individual pathway and microelectrode performance. The inability to draw such definitive conclusions is due to the fact that multiple pathways play a role simultaneously in propagating neuroinflammation following microelectrode implantation [22, 23]. In order to draw such conclusions, the field must begin to look at transgenic ‘knock-out’ or ‘knock-in’ mouse models.

In contrast to rat models, transgenic mouse models have gained popularity in the biosciences for mechanistic studies aided in the discovery of novel therapeutics. For example, using an Alzheimer's disease (AD) mouse model, Cramer *et al.* recently reported on therapeutics capable of rapidly clearing amyloid plaques [24]. Additionally, the use of a mouse model lacking superoxide dismutase has resulted in the development of therapeutics for amyotrophic lateral sclerosis and AD [25-27].

As the intracortical microelectrode fields moves closer to identifying a specific gene, cell type or neuroinflammatory pathway, transgenic mouse models may provide definitive answers to factors associated with mitigating device failure. In order to investigate a new animal model for the application of intracortical microelectrodes, it is critical establish a

comparative baseline between the widely accepted rat model and the inevitable mouse model. Hence, the goal of the current study was to compare neuroinflammation to implanted intracortical microelectrodes between the rat and the mouse model. In this study, we focused our analysis on the quantification of the most common immunohistological markers used in the field, at both initial (2 weeks) and chronic (16 weeks) time points post implantation.

2. Materials and Methods

2.1 Animals and Surgical Implantation

All procedures and animal care practices for both animal models utilized in this study were done in accordance with the Case Western Reserve University Institutional and Animal Use and Care Committee (IACUC). Rats were obtained from Charles Laboratory and age-matched to 7-8 weeks of age (∼200-250g) at the time of surgery. Similarly, C57-BL6 mice were obtained from Jackson Laboratory and age-matched to ∼6 weeks of age (∼20 g) at the time of surgery.

Surgical procedures followed our previously published protocols for both animal models [21, 28, 29]. Briefly, rats were anesthetized with a mixture of ketamine (80 mg/kg) and xylazine (10 mg/kg) administered by intraperitoneal (IP) injection and maintained on anesthesia using isofluorane (1-2%) for the duration of the surgery. Similarly, mice were anesthetized with isofluorane (3-5%) and maintained at 1-2% throughout the surgery. Following administration of anesthesia, the surgical area was shaved and the animal was mounted onto a stereotaxic frame. A subcutaneous (SQ) injection of Marcaine (∼100μl; 0.25%) was then administered below the incision site as a local anesthetic. To ensure a sterile surgical field, the shaved surgical site was scrubbed with alternating passes of betadine and 70% isopropanol. It is also important to note, that all surgical procedures for mice were performed in a class II sterile hood using microisolator techniques. To prevent retinal drying, ophthalmic ointment was used throughout the surgery. Additionally, prior to surgery all animals received the antibiotic cefazolin (16 mg/kg) and analgesic meloxicam (1 mg/kg (rats), 4 mg/kg (mice)) by SQ injection to prevent infection and manage pain, respectively.

An incision was created down midline until lambda and bregma were visible, and the surrounding tissue was retracted to expose the skull. The skull was penetrated using a biopsy punch (P/N #536, PSS Select) to create 3-mm hole, exposing the brain tissue (3 mm lateral to the midline and 4 mm caudal to bregma (rats); 1 mm lateral to the midline and 2 mm caudal to bregma (mice). For rats, the dura was then reflected manually using a 45° dura pick. Dura reflection was not nece ssary for mice. A non-functional single shank 'Michigan'-type electrode (2 mm × 123 μm × 15 μm) was then slowly inserted into cortical tissue by hand in both animal models, while taking precaution to avoid any visible vasculature. Microelectrodes were implanted approximately 2 mm into the cortex and implant orientation was maintained across all surgeries. All implanted electrodes used in this study underwent ethylene oxide (EtO) gas sterilization [28]. Prior to implantation, all electrodes were degassed for a minimum of 12 hours. Following electrode placement, kwik-sil (World Precision Instruments) was applied over the exposed cortical tissue to prevent cortical drying. Inserted electrodes were then securely anchored to the skull using ultra-

violet (UV) curing dental acrylic (Fusio/Flow-it ALC, Pentron Dental). Finally, the incision site was closed using 5-0 monofilament polypropylene suture and topical triple antibiotic ointment was applied over the sutured area to prevent drying and infection.

2.2 Tissue Extraction and Processing

The neuroinflammatory response to intracortical microelectrodes between the rat and the mouse model was compared at pre-determined time points of either two or sixteen weeks [21]. Prior to perfusion, animals were heavily anesthetized with an IP injection of ketamine (80 mg/kg) and xylazine (10 mg/kg). Each animal was then transcardially perfused with 1X phosphate buffered saline (PBS) until the exudate was clear (approximately 500 mL per rat and 20 mL per mouse). Tissue was subsequently fixed with 4% paraformaldehyde (PFA). Brain tissue was carefully extracted and placed in fresh 4% PFA for 48-72 hours at 4° C until cryoprot ected.

Rat brains were then cryoprotected using a stepwise gradient of sucrose (10%-20%-30%) in 1X PBS. Mouse brains were cryoprotected in 30% sucrose in PBS for 48 hours. Following cryoprotection, both rat and mouse brains were frozen in optimal cutting temperature (OCT) medium (Tissue Tek). Brain tissue was then sliced into either 20 μm (rats) or 16 μm (mice) thick axial sections and directly mounded onto glass slides (SuperFrost Plus). All mounted sections were stored at -80°C until immunohistochemistry was performed.

2.3 Immunohistochemistry

Two critical time points (two and sixteen weeks) important in the assessment of neurodegenerative events were analyzed and compared between the two models [21, 30]. At each pre-determined end-points of two and sixteen weeks, the neuroinflammatory response was assessed between the animal models using common immunohistochemical markers used in the field [31-33].

2.3.1 Antibodies—The following primary antibodies were used to evaluate rat cortical tissue in this study: mouse anti-glial fibrillary acidic protein (GFAP) (1:500, #A-21282, Life Technologies), mouse anti-CD68 (1:100, #MAB1435, Chemicon), mouse anti-neuronal nuclei (NeuN) (1:250, #MAB377, Chemicon) and rabbit anti-immunoglobulin G (IgG) (1:100, #618601, AbD Serotec).

The following primary antibodies were used to evaluate mouse cortical tissue in this study: rat mAb to CD68 [FA-11] (1:500, ab53444, Abcam), GFAP polyclonal rabbit antiserum (1:500, RA22101, Neuromics), rabbit anti-Ms lgG (1:1000, STAR26B AbD Serotec), and mouse anti-NeuN clone A60 (1:250, MAB377, Millipore).

2.3.2 Immunofluorescent Antigen Tissue Labeling—Immunohistochemistry was performed using previously established methodology [28, 29]. Briefly, tissue sections were removed from -80°C and were equilibrated to room temperature (RT) for approximately 15 minutes. Tissue was then washed three times with 1X PBS to remove remaining OCT and permeated with 1X PBS with 0.1% Triton-X 100 (Sigma) (1X PBS-T) for 15 minutes. Tissue sections were then incubated in blocking buffer (4% v/v serum, 0.3% v/v Triton-X

100, 0.1% w/v sodium azide) for 1 hour at RT. To stain rat tissue sections, goat serum was used in the blocking buffer. Similarly, to stain mouse tissue sections, chicken serum was used in the blocking buffer. Next, primary antibodies (diluted in blocking buffer) were added to tissue sections and incubated for 18-22 hours at 4°C.

Unbound primary antibodies were then removed using six subsequent washes with 1X PBS-T. Next, species-specific secondary antibodies (anti-rabbit, anti-goat, anti-mouse or anti-rat Alexa-Fluor 488 and anti-rabbit, anti-goat or anti-mouse Alexa-Fluor 594, Molecular Probes) were diluted 1:1000 in blocking buffer and incubated with tissue sections for two hours at RT. Total cell population was also labeled in all tissue samples using 4′,6-diamidino-2-phenylindole (DAPI, Life Technologies). Following secondary incubation, unbound secondary antibody was removed using six subsequent washes with 1X PBS-T. Next, detergent (Triton-X) was removed with an additional three washes with 1X PBS. Additionally, tissue autofluorescence was removed using a 10 minute treatment with 0.5 mM copper sulfate buffer (50 mM ammonium acetate, pH 5.0) [29]. Finally, slides were thoroughly rinsed with ddH_2O and coverslipped using Fluoromount-G (Southern Biotech). All slides were air dried at RT at then stored in the dark at 4 °C.

2.3.3 Chromagenic Labeling of Neuronal Nuclei—For mouse tissue, neuronal nuclei densities were assessed using a Diaminobenzidine (DAB) histochemistry kit (SuperPicture Polymer DAB kit, Life Technologies) using methods previously described [28]. Briefly, tissue sections were permeated for staining as described in section 2.3.2. Sections were then blocked in blocking buffer (containing goat serum) for 1 hour at RT. Following blocking, primary antibody (diluted in blocking buffer) was added to tissue sections and incubated for 1 hour at RT. Unbound primary antibody was then removed with three washes of 1X PBS. Next, 100 μL of horseradish peroxidase (HRP) polymer conjugate was added to each tissue section for 10 minutes at RT. Unbound HRP was then removed with three washes of 1X PBS. Next, 100 μL of DAB chromogen was added to each tissue section for 5 minutes at RT. Finally, slides were thoroughly rinsed with ddH_2O, counterstained with hematoxilin, thoroughly dehydrated and coverslipped using Histomount (Life Technologies).

2.4 Imaging and Quantitative Analysis

Fluorescently stained tissue was imaged using a 10X objective on an AxioObserver Z1 (Zeiss Inc.) and an AxioCam MRm (Zeiss Inc.). In the case of DAB stained tissue, an AxioCam ERc5 color camera was used to acquire images. For all analyzed markers, a larger field of view was acquired using at least 9 individual 10X images, which were stitched together using MosaiX (Zeiss Inc.) software. In addition, for all fluorescent images, exposure times were held constant for each analyzed marker. Acquired images were exported at 16-bit tagged imaging files (TIFs) using AxioVision LE (Zeiss Inc.) software.

In this study, three quantification schemes were utilized. All markers except neuronal nuclei were quantified using an in-house, freely available, written MATLAB code (MINUTE) [29]. However, due to anatomical differences that exist between rat and mouse brain tissue, here we report on an updated version of our MINUTE software. Specifically, labeled antigens were quantified using MINUTE v1.5 (Figure 1). In the new version of the graphic user

interface, the chronic region was still defined and image intensity was still quantified in expanding 2 μm rings from the defined region of interest. In addition, however, exclusion regions were defined (if needed) to remove regions void of tissue (Figure 1D). For each marker, intensities were normalized to a background region denoting endogenous expression of labeled antigens, defined as approximately 600 μm from the interface.

Normalized intensity curves were also curve fitted using a freely available software, ezyfit, following our previously reported methods, to obtain the distance at which 63% of the total area of the curve had occurred (lambda, λ) [28, 29]. Data presentation of normalized intensity plots is shown as an average of animals ± the standard error of the mean. To enable statistical comparisons within a given model between two and sixteen weeks, the area under the normalized intensity curve was calculated at pre-determined binned intervals (0 to 50 μm, 50 to 100 μm, 100 to 200 μm and 200 to 300 μm).

Inherent differences between the rat and the mouse model are expected due to differences in tissue sectioning and immunohistochemical analysis. Therefore, in order to directly compare neuroinflammatory markers between the animal models, total percent of the cell population at pre-determined binned intervals (0 to 50 μm, 50 to 100 μm, 100 to 200 μm and 200 to 300 μm) was evaluated based on the normalized intensity curves. Specifically, the total area under the normalized intensity curve was evaluated from 0 to 500 μm for each assessed image. Then, the percentage of the total area under the curve was reported for each of the binned interval regions. Data is reported as an average of animals ± the standard error of the mean. Statistical comparisons were made between the rat and the mouse models for each time point using the evaluated percentages at each binned interval.

Fluorescently labeled neuronal nuclei (NeuN) in rat tissue was quantified using Adobe Photoshop. First, a region of interest was manually defined and expanding concentric rings at pre-determined intervals, were drawn up to 400 μm. Next, the total cell count and area within each region was manually determined. Neuronal densities were then normalized to non-surgical age-matched control animals. Control neuronal densities were determined using the same methodology as implanted tissue and are defined as 2757 ± 274 cells/mm^2 and 1815 ± 176 cells/mm^2, for two weeks and sixteen weeks in the rat model.

To quantify neuronal nuclei densities in mouse tissue, a custom MATLAB program (NERD) was used, as previously described [28]. Briefly, using the graphic user interface, the implant site was manually designated. The MATLAB code was designed to draw expanding concentric rings at pre-determined radial distances from the implant region. Next, the locations of each neuronal nuclei was user-defined and neuronal densities were calculated for each binned interval within the software. Neuronal densities were then normalized to non-surgical age-matched control animals. Control neuronal densities were determined using the same methodology as implanted tissue and are defined as 1944 ± 28 cells/mm^2 and 1841 ± 52 cells/mm^2, for two weeks and sixteen weeks in the mouse model.

For both animal models, all neuronal nuclei counts are reported as a percent to age-matched non-surgical control animal and shown as an average of animals ± the standard error of the mean.

2.5 Statistical Analysis

Statistical analysis was performed using Minitab software (Minitab, Inc) using independent animal averages (n = 5-7 animals/conditions). Pairwise comparisons were performed using a general linear one-way analysis of variance (ANOVA) model using a post-hoc Tukey test. Significance was considered as $p<0.05$.

3. Results

3.1 Activated Microglia and Macrophages (CD68)

Within the context of our study, we compared the neuroinflammatory response to intracortical microelectrodes between the rat and the mouse model. First, we investigated the presence of CD68, a cytoplasmic antigen over-expressed in activated microglia and macrophages, around the implanted microelectrode at two and sixteen weeks post implantation [34].

At both time points in the rat model, CD68+ immunoreactivity was found to be concentrated within the first 100 μm of the implanted microelectrode (Figure 2A). Additionally, we found that CD68+ immunoreactivity significantly declined from 0 to 100 μm between two and sixteen weeks in the rat model (Figure 2A). Similar CD68+ immunoreactivity was observed in the mouse model, where the peak antigen intensity was found to be within the first 100 μm of the implant (Figure 2B). However, in contrast to the rat model, the mouse model showed no significant differences in CD68+ immunoreactivity between two and sixteen weeks.

We next compared the percent distribution of CD68+ immunoreactivity up to 300 μm from the implant between the rat and mouse model (*see Section 2.4*). At two weeks, we found similar CD68+ immunoreactivity between the rat and the mouse model (Figure 2C). However, by sixteen weeks, the rat model demonstrated a more widespread distribution profile compared to the mouse model, with a significantly smaller percent $CD68^+$ immunoreactivity within the first 50 μm of the implant (Figure 2D) and a significantly larger lambda value (Table 1). Significant differences in CD68+ distribution profiles were observed up to 200 μm away from the implanted device at sixteen weeks (Figure 2D).

3.2 Activated Astrocytes (GFAP)

A leading hypothesis for increases in microelectrode impedance following implantation is related to astrocyte-mediated encapsulation (termed ‘glial scarring’ or ‘astrogliosis’) of the implanted device [35]. Astrogliosis, acting as a barrier to diffusion, has also been suggested to have a prominent role in creating a neurotoxic environment around implanted microelectrodes [36]. Therefore, we next examined the expression of glial fibrillar acidic protein (GFAP), a marker endogenously expressed in all astrocytes and up-regulated during inflammation [37].

We found a significant decrease in GFAP expression from two to sixteen weeks between 0 to 500 μm from the microelectrode-tissue interface in the rat model (Figure 3A). Additionally, lambda values in the rat model (Table 1) suggested that the scar matures and becomes more compact from two to sixteen weeks. Interestingly, the opposite trends were

noted in the mouse model. Specifically, GFAP expression was significantly lower at two weeks between 0-50 μm from the microelectrode surface, compared to sixteen weeks, in the mouse model (Figure 3B). In addition, a more diffuse glial scar, as denoted by a higher lambda value, was observed at sixteen weeks in comparison to two weeks (Table 1).

Significant differences in GFAP+ distribution profiles were observed between the rat and the mouse model at two weeks after implantation. Specifically, we found that the mouse model had a higher percent GFAP+ immunoreactivity from 0 to 50 μm away from the implant interface (Figure 3C). The rat model had significantly higher percentages of GFAP+ immunoreactivity from 100 to 200 μm compared to the mouse model (Figure 3C) at two weeks, likely due to a more diffuse scar. By sixteen weeks, however, a similar GFAP+ distribution profile was observed between animal species (Figure 3D).

3.3 Blood-Brain Barrier Diffusivity (IgG)

Activation of microglia/macrophages and astrocytes can result in the release of pro-inflammatory cytokines and molecules into the local environment that can directly influence the permeability of neighboring cortical vasculature [18]. Further, a recent study by Saxena *et al.* demonstrated a correlation between blood-brain barrier disruption and loss of recorded neuronal signals from implanted microelectrodes [38]. Therefore, given the prominent role of blood-brain barrier stability in microelectrode function, we next assessed the permeability of vasculature around implanted devices in the rat and the mouse model. Here, we investigated the presence of immunoglobulin G (IgG), a blood protein normally not found in native brain tissue. Specifically, Winslow *et al.* demonstrated that in the rat microelectrode model, IgG infiltrates cortical tissue only following damage of local vasculature [39].

In the rat model, we found similar IgG+ immunoreactivity between two and sixteen weeks post implantation (Figure 4A). In contrast, the mouse model displayed significantly less IgG + immunoreactivity at two weeks from 100 to 200 μm from the microelectrode surface, compared to sixteen weeks post implantation (Figure 4B).

Comparisons of IgG+ distribution profiles around the implant region showed no significant differences between the animal models at two weeks post implantation (Figure 4C). However, by sixteen weeks, significantly higher IgG diffusivity was observed in the rat model compared to the mouse model, as indicated by a larger lambda value (Table 1). Specifically, significant differences in IgG+ distribution profiles were observed up to 200 μm between the rat and the mouse model at sixteen weeks post implantation (Figure 4D).

3.4 Neuronal Nuclei (NeuN)

Alterations in microglia/macrophages, astrocytes and blood-brain barrier stability can directly affect the viability of the neuronal environment [19, 30]. It has also been suggested by Buzsaki *et al.*, that neuronal cell bodies must be within 50 to 140 μm of the implanted microelectrode to obtain reliable recordings [40]. Therefore, we also investigated the density of neuronal nuclei populations around implanted microelectrodes in both the rat and the mouse models. Here, we used a NeuN antibody, selectivity staining neuronal cell bodies in cortical tissue [41].

In the rat model, neuronal densities significantly increased at all binned intervals past 50 μm between two and sixteen weeks (Figure 5A-E). This is likely due to the fact that background neuronal densities were considerably higher at two weeks (2757 ± 274 cells/mm^2) compared to sixteen weeks (1815 ± 176 cells/mm^2). The opposite trend was observed in mouse tissue. In the mouse model, neuronal densities significantly decreased at all binned intervals analyzed (0-400 μm) from two to sixteen weeks. Further, background neuronal densities remained comparable between two (1944 ± 28 cells/mm^2) and sixteen weeks (1841 ± 52 cells/mm^2) in the mouse model.

At two weeks post implantation, significant differences in neuronal densities were observed between the two models from 0 to 50 μm and 200 to 300 μm from the implant (Figure 5A-E). By sixteen weeks after implantation, no significant differences were observed between the animal models (Figure 5F-J). In addition to comparisons between animal models, we also investigated statistical comparisons between a given binned interval and the background density (non-surgical age-matched sham) within each animal model. At two weeks, we found that the rat model had significantly lower densities compared to background densities from 0 to 50 μm (Figure 5E). In contrast, the mouse model demonstrated a larger neuronal 'dead-zone', with background densities not returning to background densities until beyond 100 μm (Figure 5E). At sixteen weeks, neuronal densities comparable to background densities by 50 μm away from the interface in the rat model. In contrast, the mouse model displayed significantly lower neuronal densities compared to background densities until 300 μm away from the interface (Figure 5J).

4. Discussion

Understanding the progression of neuroinflammation to intracortical microelectrodes is critical in developing neuroprotective strategies to facilitate long-term implementation of microelectrode technology. Further, identifying key mechanistic pathways that contribute to neuroinflammation could aid in the development of more favorable long-term therapeutic targets [42, 43]. To date, most studies trying to elucidate mechanisms resulting in neuroinflammation following microelectrode implantation have been conducted in rat models [14, 31, 39, 44]. However, given the ease of genetic alteration, the use of mouse models could be critical in decoupling the mechanistic pathways resulting in neurodegeneration. Hence, we conducted a quantitative assessment of neuroinflammatory events to implanted intracortical microelectrodes between a rat and mouse model.

Within our study, we noted changes in activated inflammatory cell density at the device interface (Figures 2-3). Noted differences are likely due to differences in: (1) antigen expression, (2) native cell density or (3) scaling between the two models. For example, while quantitative differences were not observed in CD68+ distribution profiles at 2 weeks post-implantation, we did note a larger intensity of activated microglia/macrophages at the interface for the rat model (Figure 2A, 2B inset). This may be due to the immunohistochemical marker used to detect the CD68+ antigen in cortical tissue. Specifically, in rat tissue, we used an ED-1 clone to CD68, which recognizes a single chain glycoprotein of 110kD that is expressed predominantly on the lysosomal membrane of myeloid cells [34]. In contrast, a FA-11 clone to CD68 was used in mouse tissue, which

recognizes mouse macrosialin, a heavily glycosylated transmembrane protein also classified as a unique scavenger receptor (ScR) family member [45]. Hence, it is possible that differences in the cellular location of CD68+ immunoreactivity influenced our observed results.

Endogenous cellular expression of all microglia/macrophages (Figure 6A-B), astrocytes (Figure 6C-D) and neuronal nuclei (Figure 6E-F) may also explain differences between the animal models. Consistent with previously reports comparing rat and mice brains [46-48], we observed that mouse tissue demonstrated notably less cellular expression of IBA-1+ immunoreactivity (total microglia/macrophages) [49], as well as GFAP+ immunoreactivity (astrocytes). Further, we noted considerable differences in neuronal densities at two weeks, of non-surgical control animals between the rat (2757 ± 274 cells/mm^2) and the mouse models (1944 ± 28 cells/mm^2) (Figure 6E, F). Specifically, at two weeks, neuronal densities were considerably higher (2757 ± 274 cells/mm^2) in the rat model compared to the mouse model (1944 ± 28 cells/mm^2).

Changes in inflammatory cell density could also be attributed to differences in the scale between the two animal models. In this study, methodology to assess neuroinflammation following microelectrode implantation was kept as similar as possible to allow for a direct comparison between the models. However, the size of the mouse brain is significantly smaller compared to the size of the rat brain. For example, several differences exist in the thickness of the cortical tissue, size of the cortical layers and the distribution of inflammatory cells within the tissue space [50] (Figure 7). In fact, Woolley et al., reported a depth-dependent neuroinflammatory response to intracortical microelectrodes [51]. Therefore, changes in cellular intensity and distribution profiles may be due to varying densities of neuroinflammatory cells down the shank of the microelectrode between the animal models.

Minimal differences in neuronal densities at the interface were noted between the animal models (Figure 5E). The reduction in neuronal density in the rat model at two weeks was correlated with a more diffuse glial scar around the microelectrode (Figure 3C; Table 1). Our results are consistent with other groups that have suggested that cellular compaction of the astroglial scar may play a role in limiting the diffusion of pro-inflammatory cytokines secreted by microglia and macrophages, which are key mediators in facilitating neurodegeneration [36, 52-54], as well as provide a mechanical shield to protect from micro-motion induced tissue strain [55, 56].

Release of pro-inflammatory molecules by microglia and macrophages can also directly affect the integrity of local vasculature. Following blood-brain barrier (BBB) disruption, alterations in local ionic milieu can result in alterations in neuronal conduction velocity and compromised synaptic stability [57-59]. Additionally, extravasated serum proteins have been suggested to result in a self-perpetual cycle of neuroinflammation and neurodegeneration [19]. Blood brain barrier stability has also been linked to reductions in recording quality [38].

To measure the integrity of vasculature in our study, we utilized labeling of immunoglobulin G (IgG), a serum protein not normally found in cortical tissue [60]. We observed elevated levels of IgG around the interface in both models, at both time points, indicating chronic BBB disruption. Significant differences in IgG intensity distributions were only noted between the animal models at sixteen weeks post implantation (Figure 4). We found that changes in IgG intensity distribution at sixteen weeks correlated with observed differences in CD68+ immunoreactivity between the animal models (Figure 2). Similar to previous reports [39, 61], our results suggest that activation of microglia/macrophages may play a key role in facilitating BBB stability around implanted microelectrodes.

Although a few significant differences were observed between the two models, a number of factors likely contribute to neuroinflammation to implanted microelectrodes. Specifically, we cannot discount the fact that inherent differences in surgical technique exist in both animal models. For example, the skull of the mouse is approximately 5 times thinner than the rat [62]. Therefore, it is probable that changes in pressure during skull removal could affect localized edema and possible infiltration of meningeal cells into the implantation site. In addition, as discussed in Figure 6 and Figure 7, inherent differences in the scale and physiology of the animal models could affect the observed differences in the inflammatory response following microelectrode implantation.

5. Conclusions

In this study, we found a similar neuroinflammatory response following microelectrode implantation between rat and mouse models at two and sixteen weeks post implantation. Slight variations in the neuroinflammatory response could be attributed to surgical technique and fundamental differences in anatomical/physiological processes. Here, we suggest that future researchers be aware of the key differences in the neuroinflammatory time course when moving towards using the mouse model. Particularly, it is important to keep variations between the two animal models in mind when trying to elucidate mechanistic pathways that may play a role in propagating the neuroinflammatory response. We conclude that the potential mechanistic information that can be gained by exploiting the use of transgenic mouse models far outweighs the cautionary risks that need to be accounted in the careful interpretation of data between species.

Acknowledgments

This work was supported by the Department of Biomedical Engineering and Case School of Engineering at Case Western Reserve University through lab start-up funds, the Department of Education, Graduate Fellowships in neural engineering, GAANN:P200A100112 (K. Potter), and the NIH Neural Engineering and Rehabilitation Training Grant 5T32EB004314-14 (M. Ravikumar). Additional funding on this research was supported in part by the Department of Veterans Affairs Merit Review (J. Capadona, B7122R), Presidential Early Career Award for Scientist and Engineers (J. Capadona, PECASE), and the Nation Institute of Health (J. Capadona, National Institute of Neurological Disorders and Stroke, 1R01NS082404-01A1). The authors also acknowledge J. Skousen for fruitful scientific discussions during the data collection and interpretation phase of this study, and P. Tresco for his inspirational seminar at the 2012 Neural Interfaces Conference, which partially inspired this study. Additionally, the authors would like to thank J. Skousen for scientific discussion during all phases of the project. None of the funding sources aided in the collection, analysis and interpretation of data, in the writing of the report, or in the decision to submit the paper for publication.

References

1. Schwartz AB. Cortical neural prosthetics. Annu Rev Neurosci. 2004; 27:487–507. [PubMed: 15217341]
2. Cogan SF. Neural stimulation and recording electrodes. Annu Rev Biomed Eng. 2008; 10:275–309. [PubMed: 18429704]
3. Duffau H. Brain mapping in tumors: Intraoperative or extraoperative? Epilepsia. 2013; 54:79–83. [PubMed: 24328878]
4. Oakes TR, Pizzagalli DA, Hendrick AM, Horras KA, Larson CL, Abercrombie HC, et al. Functional coupling of simultaneous electrical and metabolic activity in the human brain. Hum Brain Mapp. 2004; 21:257–70. [PubMed: 15038007]
5. Anderson ML. Neural reuse: A fundamental organizational principle of the brain. Behav Brain Sci. 2010; 33:245–66. [PubMed: 20964882]
6. Carlson KS, Xia CZ, Wesson DW. Encoding and representation of intranasal CO2 in the mouse olfactory cortex. J Neurosci. 2013; 33:13873–81. [PubMed: 23966706]
7. Kim SP, Simeral JD, Hochberg LR, Donoghue JP, Black MJ. Neural control of computer cursor velocity by decoding motor cortical spiking activity in humans with tetraplegia. J Neural Eng. 2008; 5:455–76. [PubMed: 19015583]
8. Simeral JD, Kim SP, Black MJ, Donoghue JP, Hochberg LR. Neural control of cursor trajectory and click by a human with tetraplegia 1000 days after implant of an intracortical microelectrode array. J Neural Eng. 2011; 8:025027. [PubMed: 21436513]
9. Hochberg LR, Bacher D, Jarosiewicz B, Masse NY, Simeral JD, Vogel J, et al. Reach and grasp by people with tetraplegia using a neurally controlled robotic arm. Nature. 2012; 485:372–5. [PubMed: 22596161]
10. Tresco PA, Winslow BD. The challenge of integrating devices into the central nervous system. Crit Rev Biomed Eng. 2011; 39:29–44. [PubMed: 21488813]
11. He, W.; Bellamkonda, RV. A molecular perspective on understanding and modulating the performance of chronic central nervous system (CNS) recording electrodes. In: Reichert, W., editor. Indwelling neural implants: strategies for contending with the in vivo environment. CRC Press; 2008.
12. Barrese JC, Rao N, Paroo K, Triebwasser C, Vargas-Irwin C, Franquemont L, et al. Failure mode analysis of silicon-based intracortical microelectrode arrays in non-human primates. J Neural Eng. 2013; 10:066014. [PubMed: 24216311]
13. Prasad A, Xue QS, Sankar V, Nishida T, Shaw G, Streit WJ, et al. Comprehensive characterization and failure modes of tungsten microwire arrays in chronic neural implants. J Neural Eng. 2012; 9:056015. [PubMed: 23010756]
14. Verhagen JV, Gabbott PL, Rolls ET. A simple method for reconditioning epoxy-coated microelectrodes for extracellular single neuron recording. J Neurosci Methods. 2003; 123:215–7. [PubMed: 12606070]
15. Biran R, Martin D, Tresco P. Neuronal cell loss accompanies the brain tissue response to chronically implanted silicon microelectrode arrays. Exp Neurol. 2005; 195:115–26. [PubMed: 16045910]
16. Moshayedi P, Ng G, Kwok JCF, Yeo GSH, Bryant CE, Fawcett JW, et al. The relationship between glial cell mechanosensitivity and foreign body reactions in the central nervous system. Biomaterials.
17. Karumbaiah L, Norman SE, Rajan NB, Anand S, Saxena T, Betancur M, et al. The upregulation of specific interleukin (IL) receptor antagonists and paradoxical enhancement of neuronal apoptosis due to electrode induced strain and brain micromotion. Biomaterials. 2012; 33:5983–96. [PubMed: 22681976]
18. Skousen, J.; Bolick, K.; Bridge, M.; Tresco, P. A predictive model of the foreign body response to devices implanted chronically in the central nervous system. IFESS; Banff, Alberta, Canada: 2012.
19. Potter KA, Buck AC, Self WK, Callanan ME, Sunil S, Capadona JR. The effect of resveratrol on neurodegeneration and blood brain barrier stability surrounding intracortical microelectrodes. Biomaterials. 2013; 34:7001–15. [PubMed: 23791503]

20. He W, McConnell GC, Schneider TM, Bellamkonda RV. A novel anti-inflammatory surface for neural electrodes. Adv Mater. 2007; 19:3529–33.
21. Potter KA, Buck AC, Self WK, Capadona JR. Stab injury and device implantation within the brain results in inversely multiphasic neuroinflammatory and neurodegenerative responses. J Neural Eng. 2012; 9:046020. [PubMed: 22832283]
22. Mokarram N, Bellamkonda RV. A perspective on immunomodulation and tissue repair. Ann Biomed Eng. 2013; 42:338–51. [PubMed: 24297492]
23. Mokarram N, Bellamkonda RV. Overcoming endogenous constraints on neuronal regeneration. IEEE Trans Biomed Eng. 2010; 58:1900–6. [PubMed: 21193367]
24. Cramer PE, Cirrito JR, Wesson DW, Lee CYD, Karlo JC, Zinn AE, et al. ApoE-Directed therapeutics rapidly clear -amyloid and reverse deficits in AD mouse models. Science. 2012; 335:1503–6. [PubMed: 22323736]
25. Han S, Choi JR, Soon Shin K, Kang SJ. Resveratrol upregulated heat shock proteins and extended the survival of G93A-SOD1 mice. Brain Res. 2012; 1483:112–7. [PubMed: 23000195]
26. Murakami K, Murata N, Noda Y, Tahara S, Kaneko T, Kinoshita N, et al. SOD1 deficiency drives amyloid oligomerization and memory loss in a mouse model of Alzheimer's disease. J Biol Chem. 2011; 286:44557–68. [PubMed: 22072713]
27. Liao B, Zhao W, Beers DR, Henkel JS, Appel SH. Transformation from a neuroprotective to a neurotoxic microglial phenotype in a mouse model of ALS. Exp Neurol. 2012; 237:147–52. [PubMed: 22735487]
28. Ravikumar M, Hageman DJ, Tomaszewski WH, Chandra GM, Skousen JL, Capadona JR. The effect of residual endotoxin contamination on the neuroinflammatory response to sterilized intracortical microelectrodes. J Mater Chem B. 2014 Advance Article.
29. Potter KA, Simon JS, Velagapudi B, Capadona JR. Reduction of autofluorescence at the microelectrode-cortical tissue interface improves antibody detection. J Neurosci Methods. 2012; 203:96–105. [PubMed: 21978484]
30. McConnell GC, Rees HD, Levey AI, Gutekunst CA, Gross RE, Bellamkonda RV. Implanted neural electrodes cause chronic, local inflammation that is correlated with local neurodegeneration. J Neural Eng. 2009; 6:056003. [PubMed: 19700815]
31. Polikov V, Tresco P, Reichert W. Response of brain tissue to chronically implanted neural electrodes. J Neurosci Methods. 2005; 148:1–18. [PubMed: 16198003]
32. Zhong Y, Bellamkonda R. Dexamethasone-coated neural probes elicit attenuated inflammatory response and neuronal loss compared to uncoated neural probes. Brain Res. 2007; 1148:15–27. [PubMed: 17376408]
33. Azemi E, Lagenaur CF, Cui XT. The surface immobilization of the neural adhesion molecule L1 on neural probes and its effect on neuronal density and gliosis at the probe/tissue interface. Biomaterials. 2011; 32:681–92. [PubMed: 20933270]
34. Dijkstra C, Dopp E, Joling P, Kraal G. The heterogeneity of mononuclear phagocytes in lymphoid organs: distinct macrophage subpopulations in the rat recognized by monoclonal antibodies ED1, ED2 and ED3. Immunology. 1985; 54:589–99. [PubMed: 3882559]
35. Frampton JP, Hynd MR, Shuler ML, Shain W. Effects of glial cells on electrode impedance recorded from neural prosthetic devices in vitro. Ann Biomed Eng. 2010; 38:1031–47. [PubMed: 20336824]
36. Aschner M, Sonnewald U, Tan KH. Astrocyte modulation of neurotoxic injury. Brain Pathol. 2002; 12:475–81. [PubMed: 12408234]
37. Raff MC, Abney ER, Cohen J, Lindsay R, Noble M. Two types of astrocytes in cultures of developing rat white matter: Differences in morphology, surface gangliosides, and growth characteristics. J Neurosci. 1963; 3:1289–300. [PubMed: 6343560]
38. Saxena T, Karumbaiah L, Gaupp EA, Patkar R, Patil K, Betancur M, et al. The impact of chronic blood–brain barrier breach on intracortical electrode function. Biomaterials. 2013; 34:4703–13. [PubMed: 23562053]
39. Winslow BD, Christensen MB, Yang WK, Solzbacher F, Tresco PA. A comparison of the tissue response to chronically implanted Parylene-C-coated and uncoated planar silicon microelectrode arrays in rat cortex. Biomaterials. 2010; 31:9163–72. [PubMed: 20561678]

40. Buzsáki G. Large-scale recording of neuronal ensembles. Nat Neurosci. 2004; 7:446–51. [PubMed: 15114356]
41. Mullen RJ, Buck CR, Smith AM. NeuN, a neuronal specific nuclear protein in vertebrates. Development. 1992; 116:201–11. [PubMed: 1483388]
42. Rennaker RL, Miller J, Tang H, Wilson DA. Minocycline increases quality and longevity of chronic neural recordings. J Neural Eng. 2007; 4:L1–L5. [PubMed: 17409469]
43. Shain W, Spataro L, Dilgen J, Haverstick K, Retterer S, Isaacson M, et al. Controlling cellular reactive responses around neural prosthetic devices using peripheral and local intervention strategies. IEEE Trans Neural Syst Rehab Eng. 2003; 11:186–8.
44. Winslow BD, Tresco PA. Quantitative analysis of the tissue response to chronically implanted microwire electrodes in rat cortex. Biomaterials. 2010; 31:1558–67. [PubMed: 19963267]
45. Wu J, Glimcher LH, Aliprantis AO. HCO3-/Cl- anion exchanger SLC4A2 is required for proper osteoclast differentiation and function. Proc Natl Acad Sci. 2008; 105:16934–9. [PubMed: 18971331]
46. Pintado C, Revilla E, Vizuete ML, Jiménez S, García-Cuervo L, Vitorica J, et al. Regional difference in inflammatory response to LPS-injection in the brain: Role of microglia cell density. J Neuroimmunol. 2011; 238:44–51. [PubMed: 21803430]
47. Savchenko VL, McKanna JA, Nikonenko IR, Skibo GG. Microglia and astrocytes in the adult rat brain: comparative immunocytochemical analysis demonstrates the efficacy of lipocortin 1 immunoreactivity. Neuroscience. 2000; 96:195–203. [PubMed: 10683423]
48. Savchenko VL, Nikonenko IR, Skibo GG, McKanna JA. Distribution of microglia and astrocytes in different regions of the normal adult rat brain. Neurophysiology. 1997; 29:343–51.
49. Ito D, Imai Y, Ohsawa K, Nakajima K, Fukuuchi Y, Kohsaka S. Microglia-specific localisation of a novel calcium binding protein, Iba1. Mol Brain Res. 1998; 57:1–9. [PubMed: 9630473]
50. DeFelipe J. The evolution of the brain, the human nature of cortical circuits, and intellectual creativity. Front Neuroanatomy. 2011; 5:1–17.
51. Woolley AJ, Desai HA, Otto KJ. Chronic intracortical microelectrode arrays induce non-uniform, depth-related tissue responses. J Neural Eng. 2013; 10:026007. [PubMed: 23428842]
52. Fawcett JW, Asher RA. The glial scar and central nervous system repair. Brain Res Bull. 1999; 49:377–91. [PubMed: 10483914]
53. Silver J, Miller JH. Regeneration beyond the glial scar. Nat Rev Neurosci. 2004; 5:146–56. [PubMed: 14735117]
54. Sofroniew MV. Molecular dissection of reactive astrogliosis and glial scar formation. Trends Neurosci. 2009; 32:638–47. [PubMed: 19782411]
55. Harris JP, Capadona JR, Miller RH, Healy BC, Shanmuganathan K, Rowan SJ, et al. Mechanically adaptive intracortical implants improve the proximity of neuronal cell bodies. J Neural Eng. 2011; 8:066011. [PubMed: 22049097]
56. McConnell GC, Schneider TM, Owens DJ, Bellamkonda RV. Extraction force and cortical tissue reaction of silicon microelectrode arrays implanted in the rat brain. IEEE Trans Biomed Eng. 2007; 54:1097–107. [PubMed: 17554828]
57. Abbott NJ. Inflammatory mediators and modulation of blood–brain barrier Permeability. Cell Mol Neurobiol. 2000; 20:131–47. [PubMed: 10696506]
58. Abbott NJ, Rönnbäck L, Hansson E. Astrocyte–endothelial interactions at the blood–brain barrier. Nat Rev Neurosci. 2006; 7:41–53. [PubMed: 16371949]
59. Kawano H, Kimura-Kuroda J, Komuta Y, Yoshioka N, Li HP, Kawamura K, et al. Role of the lesion scar in the response to damage and repair of the central nervous system. Cell Tissue Res. 2012; 349:169–80. [PubMed: 22362507]
60. Aihara N, Tanno H, Hall JJ, Pitts LH, Noble LJ. Immunocytochemical localization of immunoglobulins in the rat brain: relationship to the blood-brain barrier. J Comp Neurol. 1994; 342:481–96. [PubMed: 8040362]
61. Szarowski D. Brain responses to micro-machined silicon devices. Brain Res. 2003; 983:23–35. [PubMed: 12914963]
62. Paxinos, G.; Watson, C. The Rat Brain in Stereotaxic Coordinates. Academic Press;

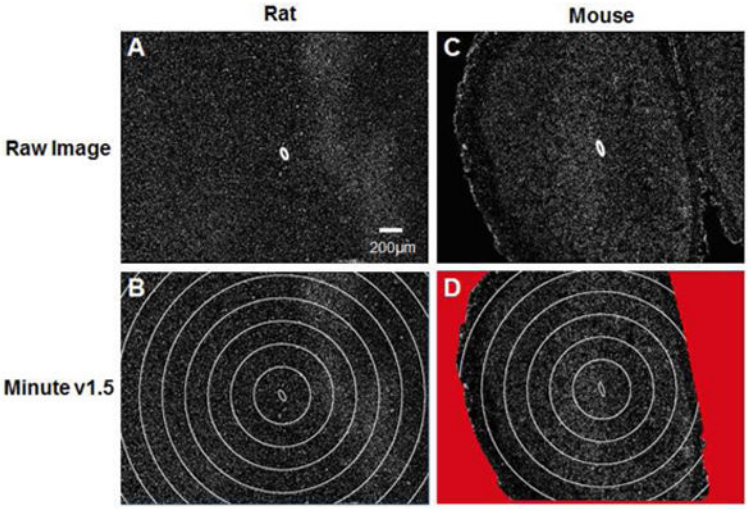

Figure 1.

Microelectrode **IN**terface **U**niversal **T**ool for **E**valuation (**MINUTE** v1.5). Within the graphical user interface, the region of interest (ROI) is defined (A/C) and expanding concentric rings are created around the ROI at a fixed radial distances of 2 μm. Here, images (B/D) are shown with expanded ellipses repeating every 200 μm for visual clarity. Within the new reported version of the software, exclusion regions can be created to remove any regions void of tissue from analysis (D).

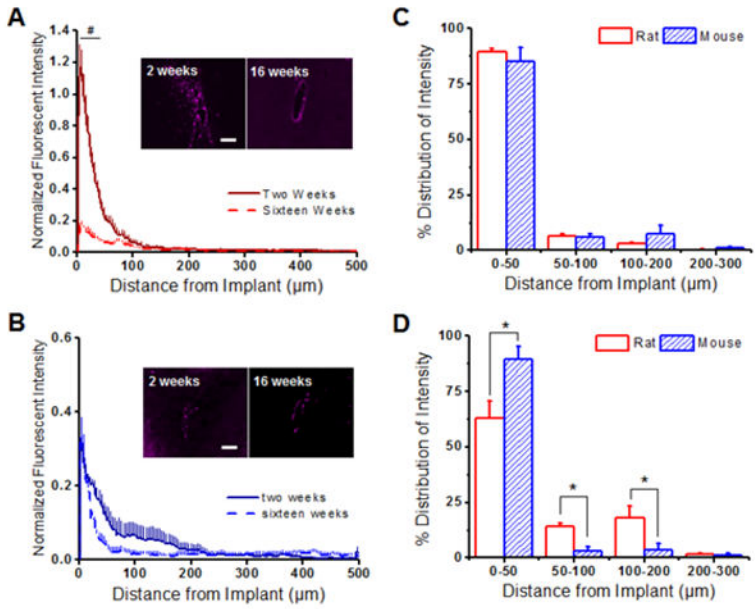

Figure 2.

Normalized CD68^{+} immunoreactivity surrounding implanted intracortical microelectrodes in the rat and the mouse model. (A) Significantly more CD68+ immunoreactivity was observed in the rat model up to 100 μm from the interface at two weeks (solid red) compared to sixteen weeks (dashed red). (B) In the mouse model, both two (solid blue) and sixteen (dashed blue) weeks demonstrated similar intensity expression profiles for CD68. (C) Comparing the percent CD68+ distribution profiles between the rat and mouse model showed no statistical differences for any investigated binning interval at two weeks post implantation. (D) However, the mouse model had significantly higher CD68+ immunoreactivity from 0-50 μm from the implanted device at sixteen weeks compared to the mouse model. *$p<0.05$; Scale = 100 μm; n = 4-7 animals for each cohort

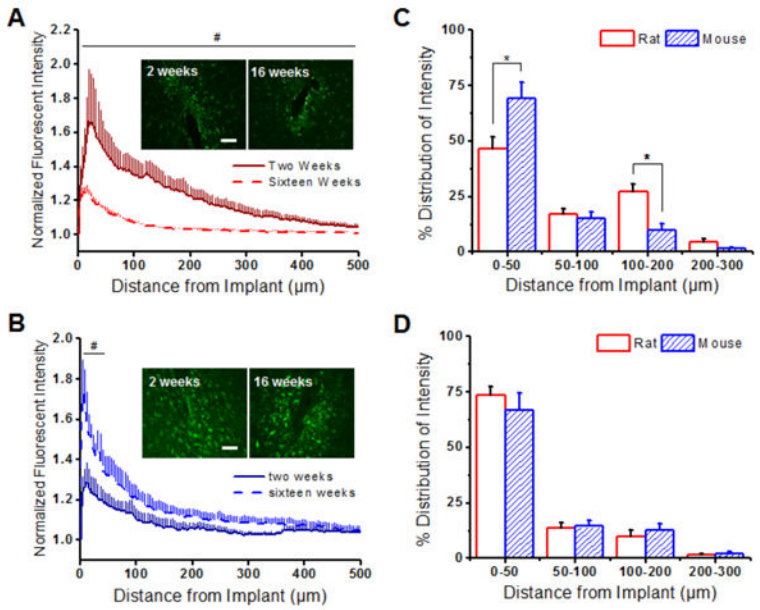

Figure 3.

Astrocytic scarring (GFAP+ immunoreactivity) around implanted intracortical microelectrodes in the rat and the mouse model. (A) GFAP+ immunoreactivity was found to be significantly higher up to 500 μm away from the implant at two weeks (solid red) compared to sixteen weeks (dashed red) in the rat model. (B) In contrast, lower GFAP+ immunoreactivity was found within the first 50 μm of the implanted device at two weeks (solid blue) compared to sixteen weeks (dashed blue) in the mouse model. (C) GFAP+ distribution profiles were significantly higher in the mouse model in comparison to the rat model at two weeks from 0-50 μm and 100-200 μm from the microelectrode-tissue interface. (D) By sixteen weeks, similar GFAP+ distribution profiles were observed between the animal models. *$p<0.05$; Scale = 100 μm; n = 4-7 animals for each cohort

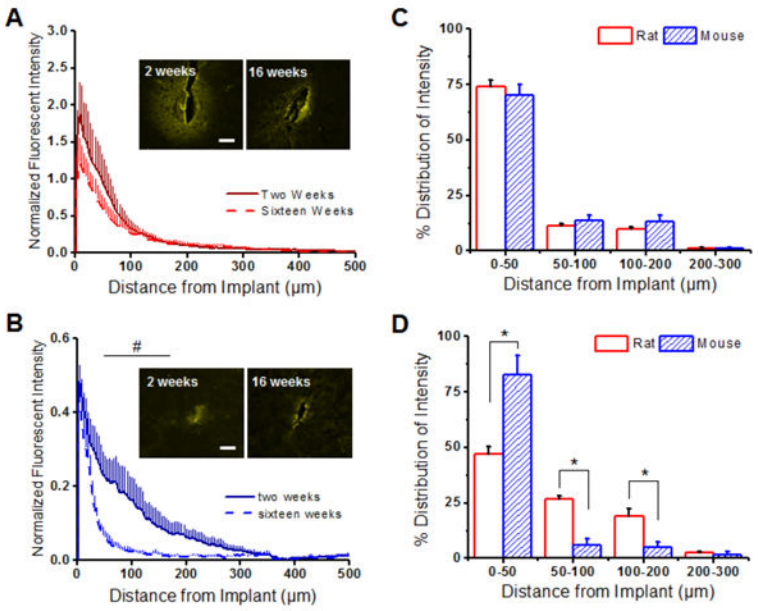

Figure 4.

Blood-brain barrier permeability (IgG) around implanted microelectrodes in the rat and the the mouse model. (A) In the rat model, similar IgG+ immunoreactivity was observed at two weeks (solid red) and sixteen weeks (dashed red). (B) In contrast, significantly more IgG+ immunoreactivity was noted from 50 to 200 μm away from the implanted device at two weeks post implantation in the mouse model. (C) Similar IgG+ distribution profiles were observed in both the rat and the mouse model at two weeks. (D) By sixteen weeks, however, a more diffuse/widespread IgG+ distribution profile was noted in the rat model (0-200 μm) compared to the mouse model. *$p<0.05$; Scale = 100 μm; n = 4-7 animals for each cohort

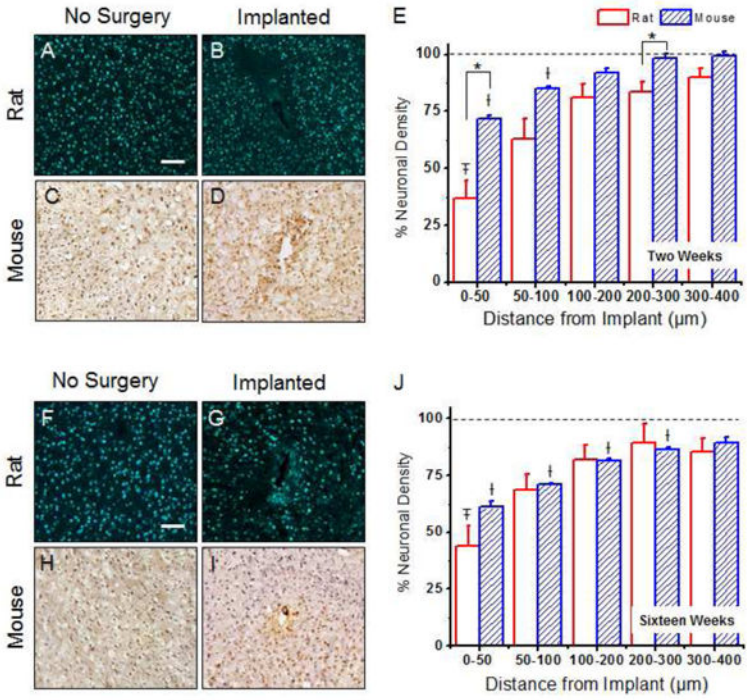

Figure 5.

Neuronal nuclei densities around implanted microelectrodes in the rat and the mouse model. At two weeks post implantation, statistical differences between neuronal densities the rat and mouse models were noted from 0-50 μm and 200-300 μm away from the implant (A-E). No significant differences were observed between the animal models at sixteen weeks post implantation (F-J). The total neuronal nuclei density was calculated for each model at two and sixteen weeks and is reported as a percent cell density to a non-surgical, age-matched sham control. Data represents an average ± s.e.m. *$p<0.003$; $^{‡}p<0.01$ vs. rat sham background; $^{†}p<0.002$ vs. mouse sham background, scale = 100μm; n = 4-7 animals for each cohort

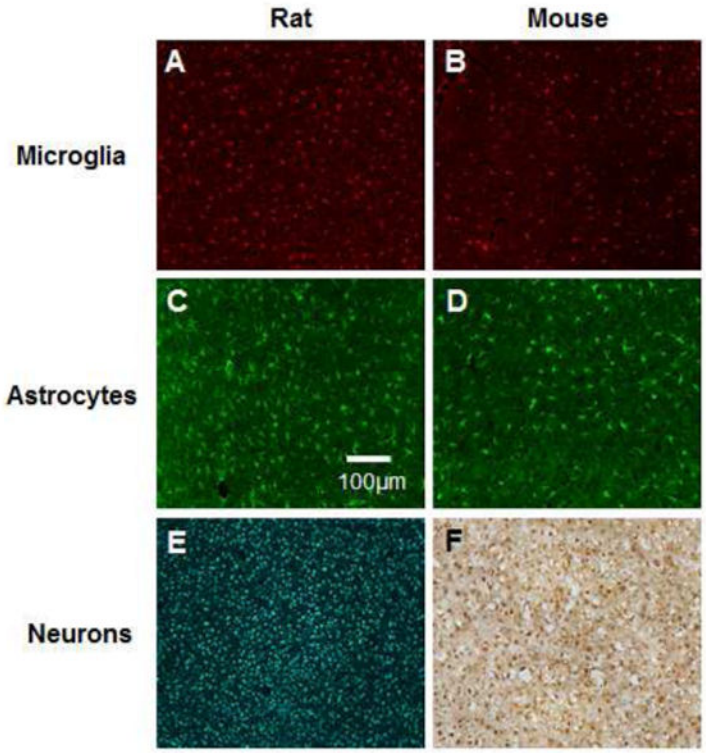

Figure 6.

Endogenous expression inflammatory cells in cortical tissue in the rat and the mouse model. Expression of microglia/macrophages (A, B), astrocytes (C, D) and neurons (E, F) in a two week age-matched non-surgery control shams. Scale bar=100 μm.

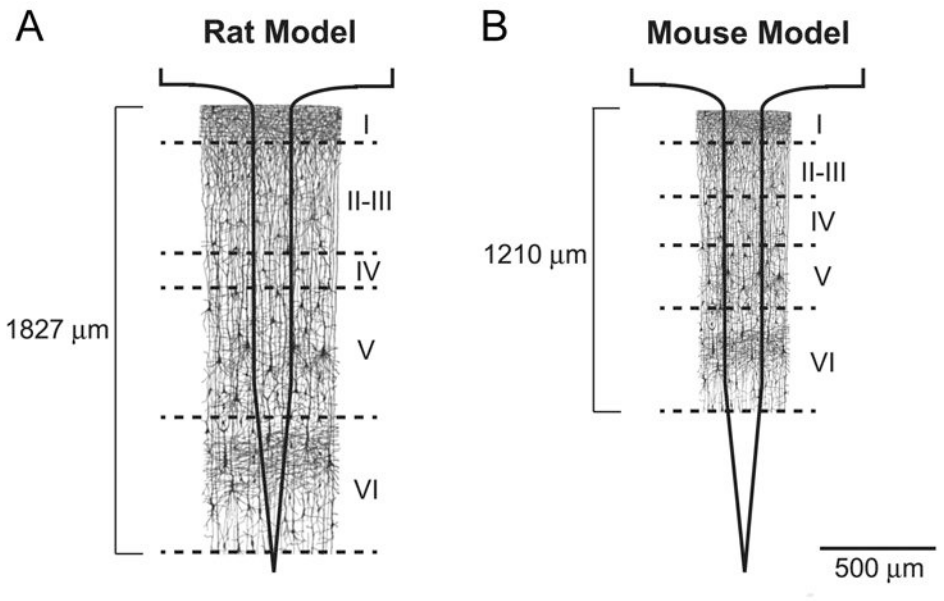

Figure 7.
Schematic illustration of differences in cortical layers between the rat and the mouse model.

Table 1
Average Lambda Values ± S.E.M for IHC Analysis Curves

	2 Weeks	16 Weeks
CD68		
Rat	41.96 ± 3.46	65.05 ± 8.38 *c*
Mouse	60.27 ± 12.72 *b*	27.53 ± 3.03 *b,c*
GFAP		
Rat	204.09 ± 29.09 *c*	134.90 ± 24.78
Mouse	55.99 ± 4.87 *b,c*	155.96 ± 31.79 *b*
IgG		
Rat	91.80 ± 8.61	91.41 ± 14.919 *c*
Mouse	117.97 ± 26.80 *b*	54.55 ± 9.59 *b,c*

Average lambda values ± S.E.M for CD68, GFAP and IgG analysis curves for the rat and mouse model at 2 and 16 weeks post implantation.

a denotes significant differences within the rat model from 2 and 16 weeks post implantation;

b denotes significances within the mouse model from 2 to 16 weeks post implantation;

c values denote significant differences between the rat and mouse model ($p<0.05$). n = 4-7 animals for each cohort